RESEARCH ARTICLE

Key Points:
- We analyze spectra of Venus's equatorial atmosphere taken during the second MESSENGER flyby on 5 June 2007
- Cloud tops are located at 75 ± 2 km in the equatorial atmosphere.
- Among all candidates proposed so far, S_2O and S_2O_2, with subindices provide the best agreement with the UV absorption retrieved here

Correspondence to:
S. Pérez-Hoyos,
santiago.perez@ehu.eus

Venus Upper Clouds and the UV Absorber From MESSENGER/MASCS Observations

S. Pérez-Hoyos[1] [ID], A. Sánchez-Lavega[1] [ID], A. García-Muñoz[2], P. G. J. Irwin[3] [ID], J. Peralta[4] [ID], G. Holsclaw[5] [ID], W. M. McClintock[5] [ID], and J. F. Sanz-Requena[6] [ID]

[1]Departamento Física Aplicada I, ETSI, Universidad del País Vasco UPV/EHU, Bilbao, Spain, [2]Zentrum für Astronomie und Astrophysik, Technische Universität Berlin, Berlin, Germany, [3]Department of Physics, Atmospheric, Oceanic and Planetary Physics, University of Oxford, Oxford, UK, [4]Institute of Space and Astronautical Science (ISAS/JAXA), Sagamihara, Japan, [5]Laboratory for Atmospheric and Space Physics, Boulder, CO, USA, [6]Departamento Ciencias Experimentales, Universidad Europea Miguel de Cervantes, Valladolid, Spain

Abstract One of the most intriguing, long-standing questions regarding Venus's atmosphere is the origin and distribution of the unknown UV absorber, responsible for the absorption band detected at the near-UV and blue range of Venus's spectrum. In this work, we use data collected by Mercury Atmospheric and Surface Composition Spectrometer (MASCS) spectrograph on board the MErcury Surface, Space ENvironment, GEochemistry, and Ranging (MESSENGER) mission during its second Venus flyby in June 2007 to address this issue. Spectra range from 0.3 μm to 1.5 μm including some gaseous H_2O and CO_2 bands, as well as part of the SO_2 absorption band and the core of the UV absorption. We used the NEMESIS radiative transfer code and retrieval suite to investigate the vertical distribution of particles in the equatorial atmosphere and to retrieve the imaginary refractive indices of the UV absorber, assumed to be well mixed with Venus's small mode 1 particles. The results show a homogeneous equatorial atmosphere, with cloud tops (height for unity optical depth) at 75 ± 2 km above surface. The UV absorption is found to be centered at 0.34 ± 0.03 μm with a full width at half maximum of 0.14 ± 0.01 μm. Our values are compared with previous candidates for the UV aerosol absorber, among which disulfur oxide (S_2O) and dioxide disulfur (S_2O_2) provide the best agreement with our results.

Plain Language Summary The atmosphere of Venus is fully cloud covered, and its clouds are very reflective in most visual wavelengths, with the exception of the near ultraviolet, where an absorber of unknown origin strongly absorbs solar radiation. Such a mysterious absorber provides contrast to many atmospheric features whose dynamics can be tracked from images, and it also has a substantial role in the energy budget of the planet. But, as of today, we have no clear idea what it is made of. In this work, we have analyzed spectra taken during the second Venus flyby of MErcury Surface, Space ENvironment, GEochemistry, and Ranging (MESSENGER) spacecraft on its route to Mercury, in 2007. Using a numerical code, we have reproduced the light reflected by the equatorial atmosphere of the planet and retrieved the distribution of particles in the upper atmosphere of Venus, with a cloud top of some 75 km above the surface. We have also retrieved the absorption spectrum of the puzzling absorber and compared it with some previously proposed candidates. While no perfect match is found, sulfur-bearing species (S_2O and S_2O_2) provide the best agreement. There is still a long way to undoubtedly identify Venus's UV absorber, but this work provides substantial spectral constraints.

1. Introduction

Venus is the only known terrestrial planet that is fully cloud covered. These clouds are optically thick in the visible wavelengths, so seeing the surface requires observations at longer wavelengths to gaze through them. However, Venus clouds themselves have been studied for more than 40 years (Esposito et al., 1983) particularly since the arrival of the first space missions (Veneras and Pioneer Venus series). Since 1962 fifteen missions have visited the planet and provided a huge amount of information (Zasova et al., 2007). However, many aspects are still missing, some of them quite important to fully understand Venusian atmospheric dynamics, chemistry, and energy budget.

The vertical distribution of clouds is one of the aspects that we now understand better. Clouds are distributed roughly from altitudes of ∼50 km up to ∼70 km, although there are hazes that can be found both above and below such levels (Esposito et al., 1997). We know since the 1970s that most of the visible light is scattered by spherical particles of 1 μm radius composed of a liquid mixture of water and sulphuric acid at 75% concentration (Hansen & Hovenier, 1974). This particle distribution is responsible for distinct features such as the primary rainbow and the glory that can be seen even in the disk-integrated reflecting properties of the planet (García-Muñoz et al., 2014; Hansen & Hovenier, 1974). Many recent works have reported the photometric or polarimetric glory observations on Venus clouds (Petrova et al., 2015; Rossi et al., 2015; Shalygina et al., 2015). Such particles are accompanied by other statistical modes whose vertical distribution and overall latitudinal variation are well known in general terms, although systematic analysis of their temporal and spatial variation is still lacking.

The aspect of Venus's clouds is bland and featureless in most wavelengths, but, when observed in the near ultraviolet, particularly at 0.36–0.37 μm, lots of structures emerge (Peralta, Lee, McGouldrick et al., 2017) revealing the dynamics at Venus upper clouds. In fact, it was the UV observations of Venus (Ross, 1928) that revealed its westward atmospheric superrotation (Boyer & Camichel, 1961). A number of spacecraft and ground-based facilities have taken advantage of this spectral range to investigate Venus dynamics: Mariner 10 (Murray et al., 1974), Pioneer Venus (Rossow et al., 1980), Galileo (Belton et al., 1991), and Venus Express (Bertaux et al., 2016; Khatuntsev et al., 2013; Titov et al., 2012), to name a few. In recent times, it has been possible to use modest aperture telescopes to provide support to JAXA's Akatsuki mission (Sánchez-Lavega et al., 2016). There is also some degree of cloud top contrast in near-infrared images, mostly caused by different scattering properties below the cloud tops (Crisp et al., 1986; Takagi & Iwagami, 2011).

The UV tracer is also discernible in the spectra of the planet, with a broad absorption band in the near-UV and blue side of the spectrum, roughly from 0.28 μm to 0.5 μm (Pollack et al., 1980). Given its unknown origin, it is sometimes referred to as the "mysterious UV absorber." SO_2 was initially suggested as a candidate, but it only contributes to short-wavelength absorption and its effect is negligible at wavelengths longer than 0.32 μm (Blackie et al., 2011), so another species is required. During the last decades, sulfur-bearing species have been often suggested as candidates for the unknown absorber (Pollack et al., 1980; Toon et al., 1982), but an unambiguous identification is still missing. Very recently, disulfur dioxide has been proposed as the mysterious absorber (Frandsen et al., 2016), in the form of the isomers *cis*-OSSO and *trans*-OSSO, as the calculation of their properties matches the spectral signature of the absorption and makes a plausible case for the chemistry required for their formation. Other authors have proposed different species over the years (Zasova et al., 1981), and some of these candidate species have been backed by detailed chemistry models (Krasnopolsky, 2016) that provide reasonable sinks and sources for the required products . As of today, there is no general agreement on the nature of the UV absorber in Venus, and thus this remains as one of the most intriguing open questions in planetary atmospheres (Krasnopolsky, 2006). An excellent review of a good number of candidates proposed so far can be found in Mills et al. (2007), and a short list is given in Table 3 in section 5.2.

Venus's clouds and the UV absorber also have a direct influence on the planetary energy budget. Even though Venus is closer to the Sun and receives more solar flux than the Earth, the thick cloud cover scatters and/or absorbs more than 50% of it above 64 km (Tomasko et al., 1980). This produces an intense heating of 8 K/day (Crisp, 1986) that has been proposed to be one of the engines of the atmospheric superrotation through the excitation of thermal tides. Models based on Venus Express observations (Lee, Titov, et al., 2015) show that variations in the scale height of small aerosols create significant changes in the radiative forcing, with a vertical extension of the upper cloud layer implying a decrease of the outgoing thermal flux and enhancement of the mesospheric cooling. The global energy budget of the planet has been recently revisited by a complete reanalysis by Haus et al. (2015, 2016). In any case, it is obvious that a good characterization of the absorption in the range from 0.32 μm to 0.5 μm is essential if we want to understand the planetary energy budget and therefore Venus's dynamics.

The goal of this paper is to study the vertical distribution of particles in the mesosphere of Venus using data obtained during the second flyby of the MErcury Surface, Space ENvironment, GEochemistry, and Ranging (MESSENGER) spacecraft in route to Mercury. We will analyze near-UV to near-infrared spectra taken at the equatorial region of the planet on 5 June 2007. We will particularly focus on the absorption properties of the mysterious UV absorber in order to compare our results with currently proposed candidates for the absorption.
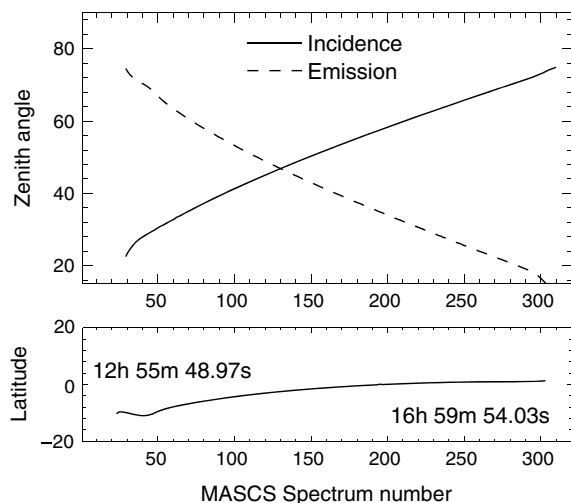
Figure 1. MESSENGER/MASCS observing conditions on 5 June 2007: (top) Incidence and emission zenith angles for all spectra analyzed here. (bottom) Mean latitude of each spectrum. Local times for the first and last spectra are also indicated.

The paper is organized as follows. We describe the data in section 2, where we discuss the spatial and spectral behavior of the measurements, as well as some cross-calibration issues between the visible and near-infrared arms of the instrument. Section 3 is devoted to a description of our methods, in particular the radiative transfer and retrieval technique, and a description of the a priori assumptions and the free and fixed parameters of the model. Results are presented in section 4, regarding both the general cloud properties and the UV absorption. Such results are discussed in section 5, in terms of the vertical particle distribution, the UV absorber candidates, and an evaluation of the impact of the present results on the energy budget of Venus's atmosphere. Finally, we summarize our main conclusions in section 6.

2. Data

2.1. Mercury Atmospheric and Surface Composition Spectrometer/MESSENGER

In this work we have used data collected by the Visible and InfraRed Spectrograph (VIRS) in the Mercury Atmospheric and Surface Composition Spectrometer (MASCS) instrument on board NASA's MErcury Surface, Space ENvironment, GEochemistry, and Ranging (MESSENGER) mission. A complete description of the instrument can be found in McClintock and Lankton (2007). VIRS uses two different detectors for visible (VIS, 0.3–1.05 μm) and near-infrared wavelengths (0.85–1.45 μm), although there is a gap in the calibrated data that leaves no overlap between channels. Both channels have a resolution of 4.7 nm and a dispersion of 2.33 nm per pixel.

MESSENGER performed its second Venus flyby in early June 2007 (McNutt et al., 2008). This was a gravity assist maneuver in order to put the spacecraft in an orbit closer to the Sun. During this process, the greatest acceleration of the mission was attained. VIRS data were acquired at a quite constant rate from 22:55 UTC to 23:02 UTC as MESSENGER moved from close to the subsolar longitude (12:50:25 local time, longitude −88.72°) to the terminator (16:54:34 LT, longitude −160.4°) along Venus's equator with a phase angle close to $\alpha \sim 90° \pm 0.5°$. This implies a length of the footprint of almost 7,500 km from the beginning to the end of the data acquisition. Figure 1 shows the incidence and emission angles and the latitude footprint of the ∼300 usable spectra. Here we have removed a few spectra with extreme viewing or illumination angles (zenith angles >75°) that will not accommodate the plane-parallel approximation of our radiative transfer model, described in section 3. Additionally, 12 spectra were removed due to low signal for unknown reasons, resulting in 318 spectra. The average size of the footprint on Venus cloud tops is ∼0.1° in latitude and ∼0.2° in longitude. Almost simultaneously, some images were also taken with the Mercury Dual Imaging System (MDIS) (Hawkins III et al., 2007) that will be used for VIS and near-infrared (NIR) channels cross calibration in section 2.3.

2.2. Data Overview

The spectrum of Venus in our wavelength range is dominated by a few species. An illustrative review of the transmission spectrum of Venus, seen as a transiting exoplanet, can be found in Ehrenheich et al. (2012, Figure 2) and García-Muñoz and Mills (2012). Starting at the shortest wavelengths, SO_2 has a maximum absorption at around 0.3 μm and then decays rapidly toward 0.32 μm (Blackie et al., 2011), where its effect is mostly negligible. Immediately afterward, there is a wide band ending well past 0.5 μm which is caused by the mysterious UV absorber extending into the blue. The rest of the bands in our range are mostly caused by H_2O, in spite of its low abundance (see Table 1), with the notable exception of the CO_2 band around ∼ 1.4 μm. This is a rather weak CO_2 band compared to others at longer wavelengths, but the massive presence of this gas makes it a prevalent constituent in our spectra. CO_2 overlaps with water also at ∼ 1.4 μm (and, to a minor extent, at other wavelengths), but H_2O displays in general wider bands.

In the following, we will use for the measurements indistinctly the radiance (expressed, e.g., in $W\,m^{-2}\,sr^{-1}\,\mu m^{-1}$) and the reflectivity. Reflectivity I/F (Sánchez-Lavega, 2011) is defined as the ratio between the observed radiance and $\pi F_\odot$ where $F_\odot$ is the solar flux (Colina et al., 1996) at normal incidence at Venus's distance.

As a first approach to the data, we fitted the observed dependence of the reflectivity with the illumination and viewing angles by using a simple Minnaert law (Minnaert, 1941). This empirical law reproduces the reflectivity

Table 1
Parameters of the Atmosphere

| Layer	Parameter	A priori	Type	Reference
Gas	$vmr(CO_2)$	0.965	Fixed	von Zhan and Moroz (1983)
	$vmr(N_2)$	0.035	Fixed	von Zhan and Moroz (1983)
$z > 70$ km	$vmr(H_2O)$	1 ppm	Fixed	Fedorova et al. (2008)
$z < 45$ km	$vmr(H_2O)$	30 ppm	Fixed	Tsang et al. (2010)
	$vmr(SO_2)$	500 ppb	Fixed	Marcq et al. (2013)
UV absorber	$m_i(\lambda)$	see Reference	Free	Pollack et al. (1980)
Mode 1	z_1 (km)	60	Free	Crisp (1986)
	τ_1	4	Free	Crisp (1986)
	$H_1(H_g)$	1	Free	Tsang et al. (2010)
	r_1, σ_1	0.3 μm, 0.44	Fixed	Barstow et al. (2012)
Mode 2	z_2 (km)	60	Free	Tsang et al. (2010)
	τ_2	8	Free	Tsang et al. (2010)
	$H_2(H_g)$	1	Free	Tsang et al. (2010)
	r_2, σ_2	1.0 μm, 0.25	Fixed	Barstow et al. (2012)
	$m_r, m_i(\lambda)$	75% H_2SO_4	Fixed	Palmer and Williams (1975)
Mode 2'	$z_{2'}$ (km)	45	Free	Tsang et al. (2010)
	$\tau_{2'}$	8	Free	Tsang et al. (2010)
	$H_{2'}(H_g)$	1	Free	Tsang et al. (2010)
	$r_{2'}, \sigma_{2'}$	1.4 μm, 0.21	Fixed	Barstow et al. (2012)
	$m_r, m_i(\lambda)$	75% H_2SO_4	Fixed	Palmer and Williams (1975)
Mode 3	z_3 (km)	45	Free	Tsang et al. (2010)
	τ_3	9	Free	Crisp (1986)
	$H_3(H_g)$	1	Free	Tsang et al. (2010)
	r_3, σ_3	3.65 μm, 0.25	Fixed	Barstow et al. (2012)
	$m_r, m_i(\lambda)$	75% H_2SO_4	Fixed	Palmer and Williams (1975)

as a function of the cosines of the incidence (μ_0) and emission (μ) angles:

$$(I/F) = (I/F)_0 \mu_0^k \mu^{k-1} \tag{1}$$

In equation (1), $(I/F)_0$ is the geometry-corrected nadir-viewing reflectivity and k is the limb-darkening coefficient. A Lambertian surface, for example, would have a value of $k = 1$.

The data provide a good fit to this expression within the observed range of viewing and illumination conditions, and the resulting limb darkening as a function of wavelength is shown in Figure 2. It is interesting to note that there are three distinct regions. Starting from longer wavelengths, above 0.5 μm limb darkening ranges $k = 1.35 – 1.40$. There is a transitional part of the spectrum where the UV absorber dominates and k is reduced down to values of 1.05. Finally, closer to the SO_2 absorption band, the limb-darkening coefficient reduces again and gets closer to Lambertian values and the observed radiance is diffuse, independent of the observation angle. This is valid for the Sun–Venus–spacecraft configuration at the moment of the flyby and would require more diverse observation conditions to be generalized. While MASCS cannot provide as much spatial resolution as an imaging device, this piece of information is very interesting when normalizing the radiance at a given wavelength to study the dependence on scattering angle, as done, for example, by Petrova et al. (2015) and Shalygina et al. (2015).

This analysis suggests that our data have a low spatial variability. In order to further investigate this aspect, we performed a principal component analysis
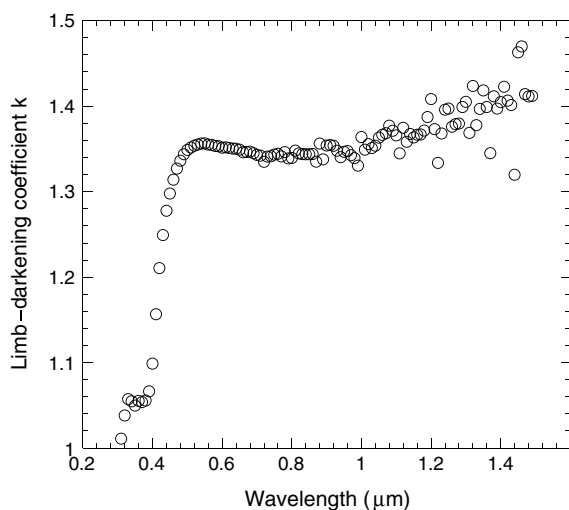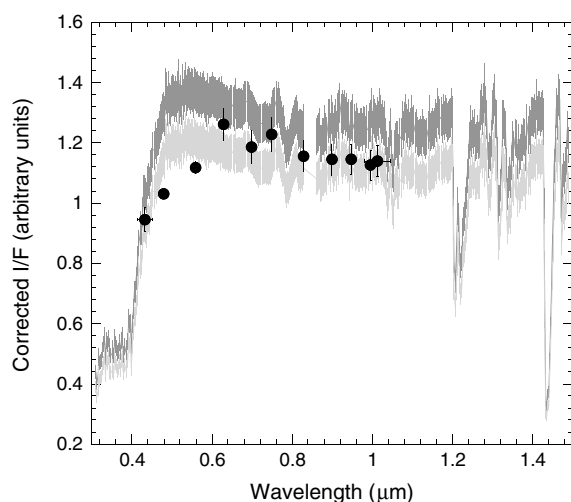
Figure 2. Limb-darkening coefficient k as a function of wavelength.
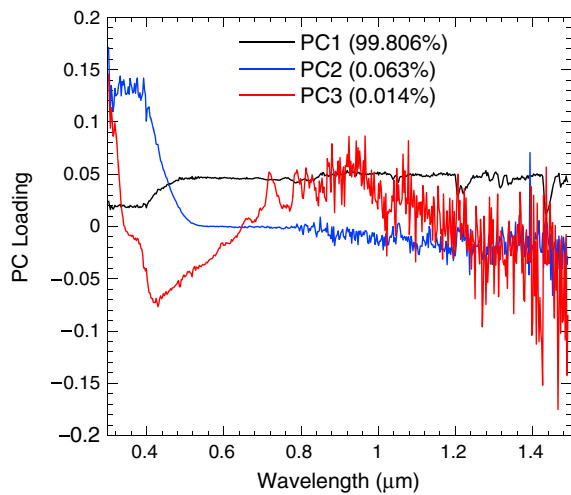
Figure 3. Loadings of the three first principal components, which account for 99.883% of the variance. The following PCs account for less than 0.002% of the variance each.

(PCA; Murtagh & Heck, 1987). The PCA provides orthogonal (independent) contributions to the absolute variance and hence is able to disentangle the spectral contribution to spatial variability. Figure 3 shows the spectral loading of each of the three first principal components. The first component PC1 accounts for more than 99.8% of the spatial variance of the MASCS spectra analyzed here. It resembles a common Venus spectrum (or the normalized average of the spectra) with the signature of SO_2 in the shortwave side, the UV absorber, and the H_2O and CO_2 bands included in this spectral range. This implies that all the variability affects all wavelengths equally, and therefore it can be assumed that variability is due to geometrical effects alone and it is basically the limb darkening presented previously. The second component PC2 has a broad signature that is well correlated with the expected UV absorption. However, PC2 only accounts for 0.06% of the variance, and hence, even though this is the strongest isolated source of variability, its contribution to the total variance is very low. Component PC3 is even lower (0.014% of the total variance) and has a very noisy spectrum in the near-infrared side, but it has a clear signature that could be related to the SO_2.
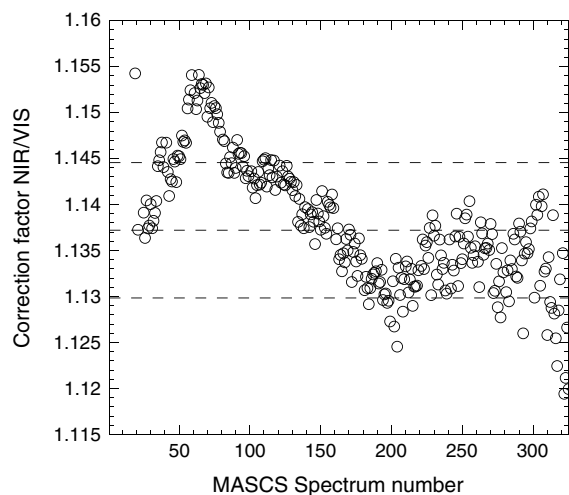
2.3. Calibration Issues

The first challenge with VIRS data is that the VIS and NIR sides of the spectrum have a cross-calibration bias. When radiances are transformed into reflectivity, the NIR side is clearly brighter than the VIS side. The calibrated spectra have a gap around ∼ 0.825 μm with no overlap between the channels (Sánchez-Lavega et al., 2016). If we compute the expected Venus spectrum by using the reasonable a priori model defined in section 3.2, we find that the continuum at both sides of the gap should be mostly the same. There should be no discontinuity in the data as the aerosol and gas optical properties do not introduce such behavior. If we focus on the 0.570–0.670 μm region for the VIS continuum and the 0.970–1.030 μm in the NIR side, models show that the NIR continuum would be 5% darker at most, depending on the model parameters. At this point, it was possible to correct the VIS spectrum to match the NIR continuum or vice versa. Initial models favored the values observed at VIS wavelengths, and the NIR spectra were brighter than expected.

In order to look for an independent confirmation, we navigated and calibrated almost simultaneous images obtained with the MESSENGER/MDIS instrument (Peralta, Lee, Hueso et al., 2017). MDIS filters only covered the VIS side of MASCS data but were in agreement with that part of MASCS data. Figure 4 shows a comparison between both instruments' averages, geometrically corrected following the method described above. While the agreement is not perfect, we decided to reduce the brightness of the NIR by a factor computed for each spectrum by evaluating the continuums described in the previous paragraph. The average correction factor was 1.137 ± 0.007, and its dependence on the spectrum number is shown in Figure 5.

This correction also has an impact on the assumed error bars of the spectrum. Here we have assumed a 5% relative error in all spectra, with a minimum error in radiance of 1 mW cm^{-2} μm^{-1} sr^{-1}. This prevents an excessive weight of the lower radiance values (particularly at absorption bands) in the fitting process, relative to the continuum values. It should be noted that the error bars are not of excessive interest, as the retrieval technique is focused in the minimization of the deviation, not in its exact value. However, the relative weight of error bars can play a role in the retrieval results.

Finally, there are some broad features in the spectra that have no exact counterpart in our modeling. These are located in 0.685–0.760 μm, 0.763–0.810 μm, and 0.815–0.830 μm. Being at the end of the VIS range and, after testing some candidates to explain the absorption, no match was found and we assumed they were artifacts, similar to the ones reported by Shalygina et al. (2015) using VeX/VIRTIS. We found no agreement either between the features reported in that work and those seen here.

Figure 4. Two alternative cross calibrations of VIS and NIR sides of MASCS-VIRS spectra compared with average MDIS values (circles with error bars) taken almost simultaneously. In light gray, a correction of the NIR side to match the VIS continuum; the opposite is shown in darker gray.

Figure 5. Ratio of the NIR to VIS continuum for every MASCS spectrum. On average, NIR side is 13.7 ± 0.7% brighter than expected. Dashed horizontal lines show the average value and its 1σ standard deviation.

3. Methods

3.1. Radiative Transfer Code

We have used the radiative transfer and retrieval suite NEMESIS (Irwin et al., 2008) in order to interpret the observations. NEMESIS stands for Non-linear optimal Estimator for MultivariatE spectral analySIS, and it is based on an optimal estimator scheme (Rodgers, 2000). The radiative transfer calculations are made in the correlated-k mode from k tables precomputed from line data obtained at the HITRAN 2012 database (Rothman et al., 2013). The radiative transfer solver is based on the doubling-adding scheme (Hansen & Travis, 1974) on a plane-parallel atmosphere. The version of NEMESIS used here accepts as free parameters those describing the vertical distribution of gases and particles as well as the imaginary refractive indexes of particles as a function of wavelength.

This is the first time that NEMESIS has been used for the inversion of Venus's dayside scattered data at visible wavelengths. We tested initial results with an implementation (García-Muñoz et al., 2013) of discrete ordinates DISORT method (Stamnes et al., 1988) including multiple scattering of Venusian particles, and both codes agreed within a few percent. This NEMESIS implementation has been exhaustively tested with Venus nightside emission as shown in previous publications (Barstow et al., 2012; Tsang et al., 2008, 2010).

3.2. Model Atmosphere

Table 1 summarizes the parameters describing the atmosphere of Venus in our model. Even though the atmosphere is divided in 20 vertical layers for computational purposes, here we prefer to separate the contribution of the gas, the UV absorber, and each of the particle modes. In this table we show the fixed or initial value for each parameter as well as a reference supporting the choice.

The role of the gas is defined by its scattering and absorption properties. Rayleigh scattering cross section as a function of wavelength was computed for a mixture of CO_2 and N_2 (Tsang et al., 2010). In the wavelength range of VIRS data there are absorption bands from CO_2 and H_2O. Line data for them was retrieved from HITRAN 2012 database and transformed to k tables. As already explained, the SO_2 plays a substantial role at the UV side of the spectrum. Absorption cross-section values of SO_2 were taken from Blackie et al. (2011). The abundance of the main consituents were taken from von Zhan and Moroz (1983). The variation of water abundance with altitude followed a simple model, with a high-altitude value taken from Fedorova et al. (2008) and a low-altitude one from Tsang et al. (2010). Between 45 and 70 km values were interpolated linearly in altitude. The SO_2 abundance is known to vary with altitude (Belyaev et al., 2012, 2017; Fedorova et al., 2008), but initial runs showed this subtlety to have little impact on the model results, so we decided to use a constant SO_2 abundance. We leave the analysis of the SO_2 vertical profile as a future work. In addition, since its abundance is highly variable with time, we used the values inferred by Marcq et al. (2013) for 2007.

The particles require a more sophisticated description. All modes except mode 1 were assumed to be composed of an aqueous solution of H_2SO_4 concentrated at 75%, whose refractive index (real and imaginary parts) were taken from Palmer and Williams (1975). We followed here the approximation of having the UV absorber well mixed with the smallest particles (mode 1), as done in other previous works (e.g., Crisp, 1986). This way, for mode 1 particles we only need the imaginary part of the refractive index to model the UV absorption. The real part of the refractive index is computed using the Kramers-Kronig relation, taking as a reference the real refractive index of H_2SO_4 at 0.5 μm. As initial values, we took the results by Pollack et al. (1980) for the same approximation.

The particle modes are distinguished by the particle size and vertical distribution. Regarding size distributions, we opted to follow the values listed by Barstow et al. (2012) for lognormal distributions which, in the end followed from the values by Pollack et al. (1993). In short, it is well known that at a given altitude range it is possible to find particles of various sizes (Esposito et al., 1997). The micron-sized mode 2 particles scatter most of the radiation at visual wavelengths, but slightly larger particles (the so-called mode 2') can be found at deeper levels. The two other families are the submicron-sized mode 1 and the larger particles of mode 3, which have radii of a few microns.
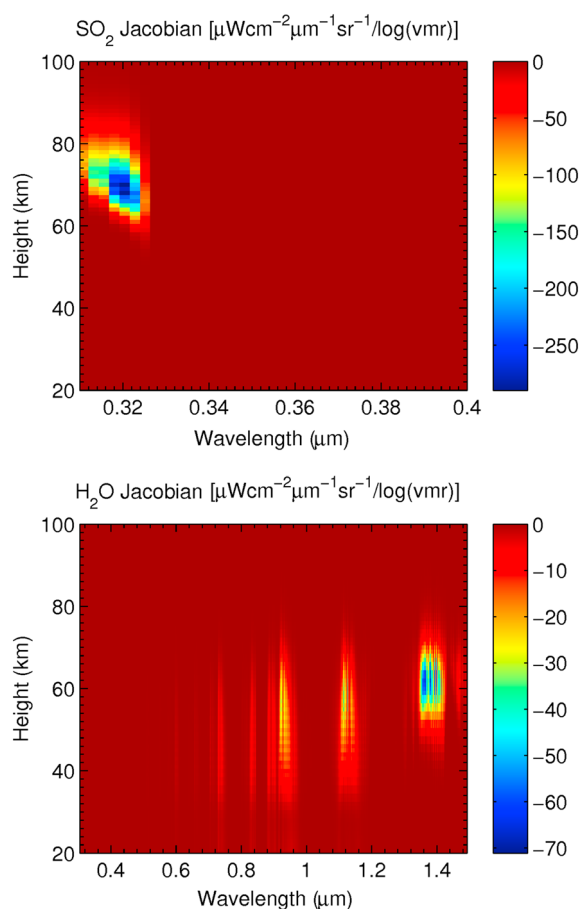
Figure 6. Jacobians for (top) SO_2 and (bottom) H_2O as a function of altitude and wavelength. Please note the restricted wavelength range used for the display of SO_2 sensitivity. Units are given in terms of radiance change per volume mixing ratio change in logarithmic units.

In order to describe the vertical distribution of such particles, we decided to follow the simplified description by Tsang et al. (2010). In this model, the distribution of particles is represented by three parameters: base altitude, scale height, and peak abundance (reached at base). The scale height refers to its value at the cloud base, and it will be given in terms of the gas scale height, which is ∼ 4 km at the cloud tops. This does not pretend to be a realistic description of the actual distribution of particles but a useful parameterization that focuses on the values that the model can constrain, as explained in section 3.3. In Table 1 we have given the total optical thickness at 0.63 μm provided by each particle mode, instead of the peak particle density, which is the parameter in the model. Hereafter we will refer to the optical thickness at this specific wavelength, except stated otherwise, in order to simplify the comparison with previous work. Also, the particle extinction coefficient (particle number density multiplied by cross section) is the most sensitive parameter for the model.

We only depart from Tsang et al.'s (2010) description of the vertical distribution of particles with mode 1. A number of forward evaluations of the a priori model demonstrated that the UV absorber should be higher in the atmosphere in order to account for the radiance at short wavelengths, leaving the rest of parameters fixed as stated in Table 1. This agreed better with the model atmosphere by Crisp (1986), so we put the a priori base altitude at $z_1 = 60$ km.

In summary, Table 1 defines a forward model that can be evaluated. When doing so, we find that it is not far from the actual data at certain geometries, particularly at intermediate illumination and viewing angles, but still requires some fine tuning that will provide useful information on the atmospheric parameters. But first, we must define which parameters are to be left as free and which ones fixed.

3.3. Free Parameters and Fitting Strategy

At this point, we need to evaluate which of the parameters that describe the atmosphere can be fitted with the current data. For doing so, we performed a number of forward evaluations, sample retrievals, and computed derivatives in order to understand the a priori sensitivity. In order to have a complete description of the model sensitivity as a function of height and wavelength, we sometimes used a continuous vertical profile with 1 km vertical resolution, instead of the parameterizations described in the preceding section.

Our initial idea was to include SO_2 and H_2O as free parameters. We show in Figure 6 the Jacobian matrix for both species (i.e., the matrix of partial derivatives of the radiance with respect to the parameter value at each altitude level). For this calculation, we assumed a constant abundance throughout the atmosphere. In the case of SO_2 we are only sensitive to concentration at altitudes 75 ± 5 km at 0.32 μm. Recent works (Vandaele et al., 2017) have shown that the vertical distribution of SO_2 above the cloud tops can be very complex, even with an inversion layer at around 70–75 km. However, our sensitivity is narrow enough to support that we are only being sensitive to SO_2 abundance at the cloud tops, even though this parameter is going to be strongly coupled with the abundance of mode 1 particles and the UV absorption in the 0.30–0.32 μm range. A future work on the SO_2 vertical profile could help to break this parameter degeneracy.

In the case of water, we have a range of sensitivities at different bands, mostly concentrated at 60 ± 10 km (particularly at 1.4 μm), but with contributions for levels as deep as 40 km and even less where the absorption band becomes weaker. This supports the need to include a better description of water with altitude, as shown in Table 1. However, sample retrievals showed very low sensitivity to both species, with dispersions and error bars larger than 200%, so we decided to fix the value of these parameters to reasonable values found in the literature, as already discussed.

Mode−1 Jacobian [μWcm^{-2}μm^{-1}sr^{-1}/log(part/g)]

Mode−2 Jacobian [μWcm^{-2}μm^{-1}sr^{-1}/log(part/g)]
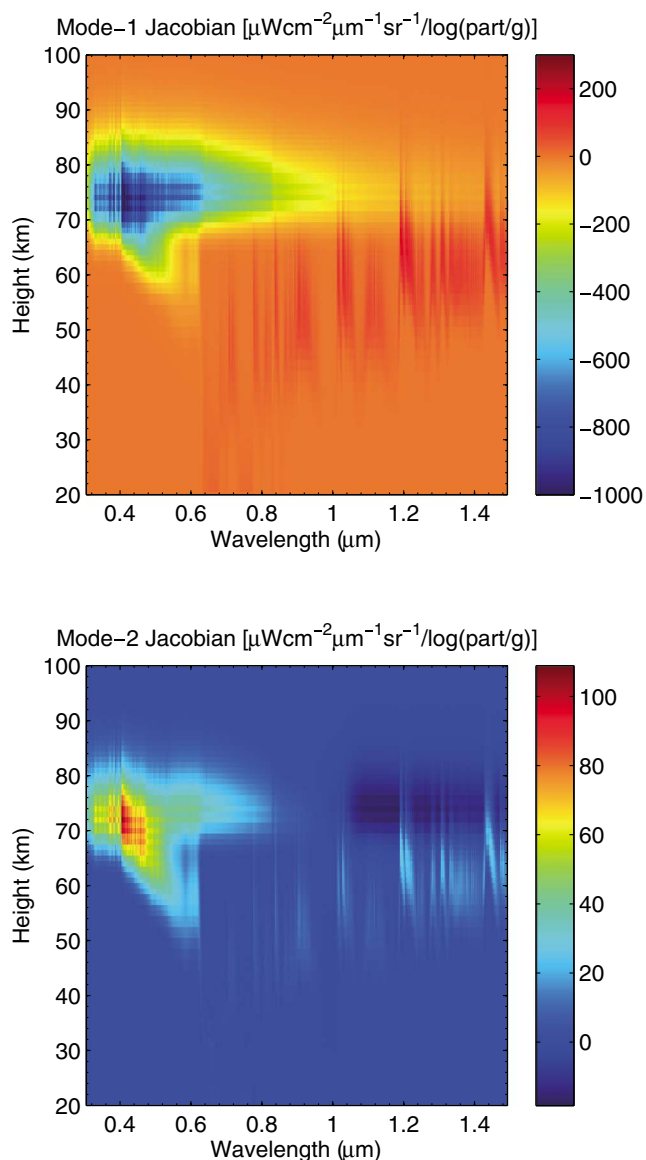
Figure 7. Jacobians for mode 1 and mode 2 particles as a function of altitude and wavelength.

In order to test the sensitivity to particle modes, we used a particle number density constant with height, instead of the parameterization presented above. This is not a realistic description of the vertical distribution, but it avoids abrupt cuts at cloud base.

The model is most sensitive to the distribution of mode 1 and mode 2 particles (Figure 7). Mode 1 is dominant at short wavelengths, where the cross section is the largest due to particle size and to having the UV absorption attached. In the near-infrared bands, mode 2 has also a strong influence. Very roughly, since the figures depend on the exact description of each cloud layer, our models are sensitive to particles in the 50–80 km range, at most, and mostly at 66 ± 6 km in the NIR bands and slightly higher, 75 ± 7 km for the UV absorption. It must be noted that our parameterization of particle distribution is defined for all atmospheric levels, while the retrieval is not necessarily reliable for all of them. Most of the radiance reflected by the planet in this wavelength range comes from the vertical levels described above, so the information on particle density above 80 km and below 50 km cannot be trusted and only the particle densities in the range of confidence can be taken as a robust conclusion of this analysis.

Regarding the simplified vertical description given in Table 1, we will see later that sensitivity is good for mode 1 and mode 2 parameters, except for their scale height. Mode 2′ and mode 3 parameters are more difficult to constrain. In order to evaluate the sensitivity of each parameter from the actual retrievals, we used an improvement factor, as defined by Irwin et al. (2015):

$$F(\%) = 100 \times \left(1 - \frac{\delta_{\text{fit}}}{\delta_{\text{apr}}} \right) \qquad (2)$$

In this equation, δ is the relative error of the a priori assumption and the fit as provided by the optimal estimator. We assumed a relative error of 25% for all parameters except for the imaginary refractive index, which is 50%. This way, an improvement factor $F = 0\%$ implies that our a posteriori relative error is the same as the prior and therefore contains less information than a retrieval with an improvement factor of $F = 100\%$, whose relative error has been reduced drastically. The actual values for improvement factors, which will justify the election of free parameters, will be given in section 4.
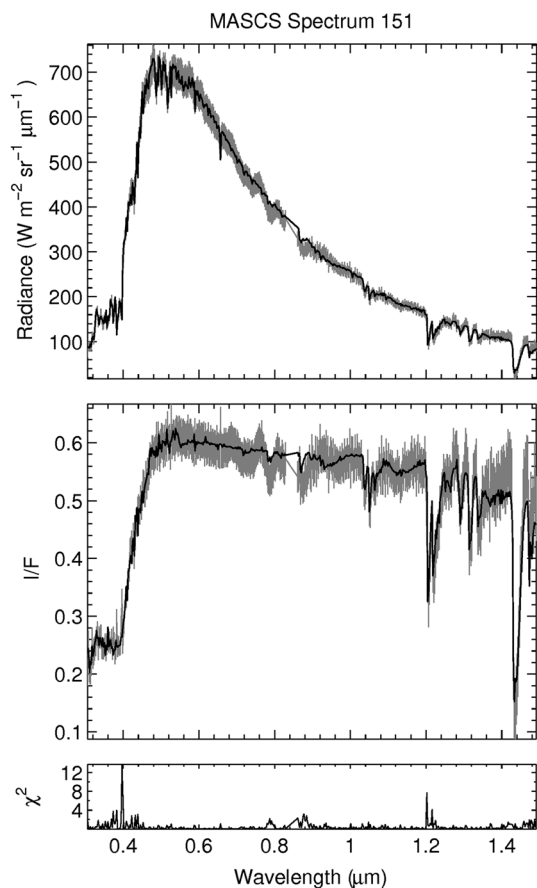
In order to avoid overfitting the imaginary refractive index, we decided to split the wavelength range into two overlapping subranges. This way, we first fitted wavelength above 0.5 μm fixing the mode 1 imaginary refractive index and leaving free the parameters of the vertical distribution of particles (12 free parameters in total). Then, the result is used as an input to fit wavelengths below 0.6 μm but now leaving free the imaginary refractive index (20 free parameters). This provides the best solution closest to our a priori for the UV absorption.

4. Results

4.1. General Comments

The strategy summarized above provides a good fit to the data, with a few exceptions. Figure 8 shows an example of fitting for an intermediate value of the illumination and viewing angles. The χ^2 value is used as a diagnostic of the goodness of the fit; it is computed as the mean quadratic deviation in terms of the error bar of the data. With respect to wavelength, the most difficult regions is the slope around 0.4 μm, where higher resolution in the imaginary refractive index would provide a better fit. The next critical region is the absorption band at 1.2 μm, where fits are in general poorer. Finally, there seems to be a systematic offset between models in the red end of the spectra, as a near-infrared continuum tends to be spectrally flatter than the models predict. We have tried nonsystematic search of alternative models with a lower slope in the near infrared with negative results. This might be a calibration issue with the spectra, maybe because of differences in the solar spectrum used (Colina et al., 1996).

Figure 8. Sample fit for MASCS spectrum 151 expressed in (top) radiance and (middle) reflectivity. Error ranges are shown in gray, and best fit model is shown in black. (bottom) The χ^2 as a function of wavelength is also shown.
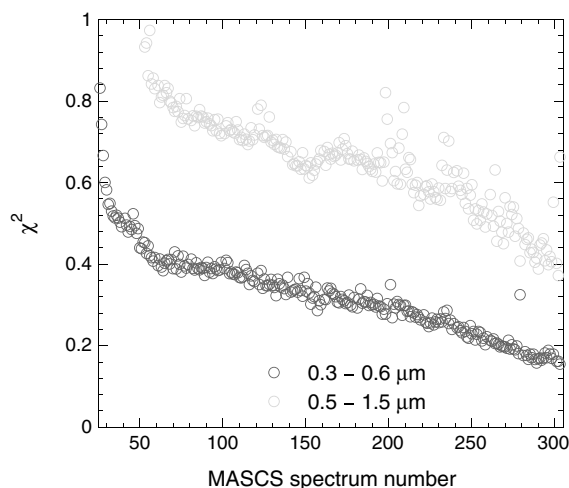
Figure 9. Mean quadratic deviation for the VIS and NIR sides of the spectrum as a function of spectrum number.

In terms of the spectrum number, the first 50 spectra are problematic. They do not converge to low values of the mean quadratic deviation (shown in Figure 9). This is particularly important in the near-infrared fitting, since fitting the ultraviolet and visible is easier when the imaginary refractive index is left as a free parameter. Such spectra are coincidentally those with higher emission angles, as shown in Figure 1. While we only filtered zenith angles greater than 75°, this suggests that the plane-parallel approximation breaks at some 70°. The model and its approximations (mainly the plane-parallel approximation) behave better at low emission angles. All in all, results for spectrum number below ∼ 60 are most likely not reliable.

4.2. Cloud Properties

Figures 10–13 show the results for the vertical distribution of each of the particle modes. All figures show the parameters (base height z, particle peak density N in particles cm^{-3}, and scale height H in terms of the gas scale height) and the improvement factor expressed as in equation (2).

Excluding spectra below number 60, mode 1 particles (see Figure 10) have a mean base height of 65 ± 2 km and maximum particle number density of 900 ± 200 particles cm^{-3}, with a scale height of 1.14 ± 0.03 H_g (∼ 4 km). The improvement factor is above 80% for the altitude, implying that the relative error has been reduced from the 25% assumed a priori to a mere 5%. The particle density and the scale height show no improvement, while for the latter the dispersion of results is lower and values are closer to the a priori. The integration of the vertical profile provides a mean optical thickness of $\tau_1 = 3.2 \pm 0.2$ at 0.63 μm, notably lower than the initial value listed in Table 1.

Results for mode 2 (Figure 11) show the base of the cloud at 56 ± 1 km with a more variable particle density of 200 ± 70 particles cm^{-3}. The scale height H_2 retrieval has a huge uncertainty, but all models converge to values substantially lower than the prior (from 1 H_g to 0.7 H_g for the best fits, with a dispersion of only 0.1 H_g). The error in z_2, as in mode 1, has been strongly reduced, and there is also some improvement in the particle density (average improvement factor of 15%). The variable number of particles results in change of the total optical thickness from $\tau_2 \sim 10$ for MASCS spectra around 50 down to $\tau_2 \sim 5.5$ for the last ones, which is a difference of almost a factor of 2.

The distribution of particles at deeper levels is more uncertain, as expected from the sensitivity analysis discussed above. Note that vertical levels above 80 km and below 50 km did not give enough sensitivity to provide a robust retrieval of the particle number density. Mode 2′ cloud base is located on average at 46 ± 2 km with a peak density of $N_2 = 70 \pm 20$ particles cm^{-3}. However, it is not expected that cloud base can be located at such deeper levels with high temperatures (McGouldrick & Toon, 2007). Results for the scale height are inconclusive. Most likely, the model is unable to separate the contribution of mode 2′ particles from that of mode 2 particles, as the particle sizes are very similar. This wavelength range does not look therefore adequate to discriminate between both modes. The integration of the particle density provides a mean optical thickness for mode 2′ of $\tau_{2'} = 6.8 \pm 0.4$, with no substantial dependence on spectrum number.

However, the contribution from mode 3 particles, which are significantly higher than mode 2 or mode 2′, seems to be more important. This is the only mode that displays a continuous variation along MESSENGER footprint, from the local noon to the evening terminator. The base height increases from 40 km to 60 km, while the average value is $z_3 = 55 \pm 2$ km.
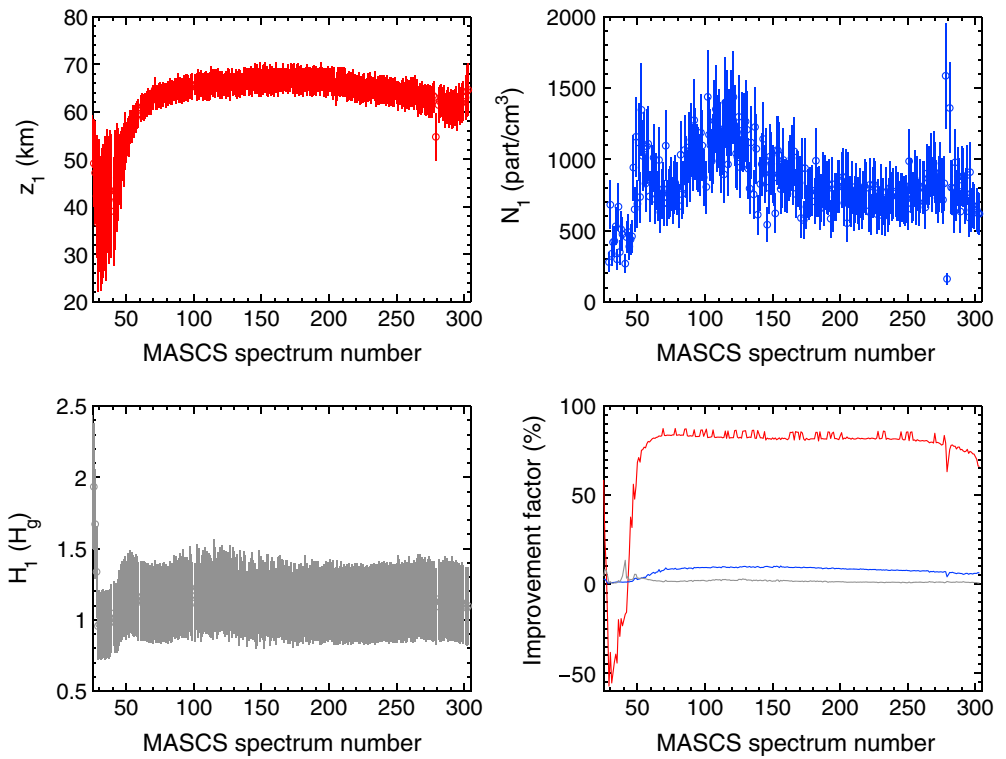
Figure 10. Model results for mode 1 particles parameters and improvement factor. Red line is used for the cloud base height z_1, blue line for the particle number density N_1, and gray for fractional scale height H_1, the scale height in terms of the gas scale height H_g.
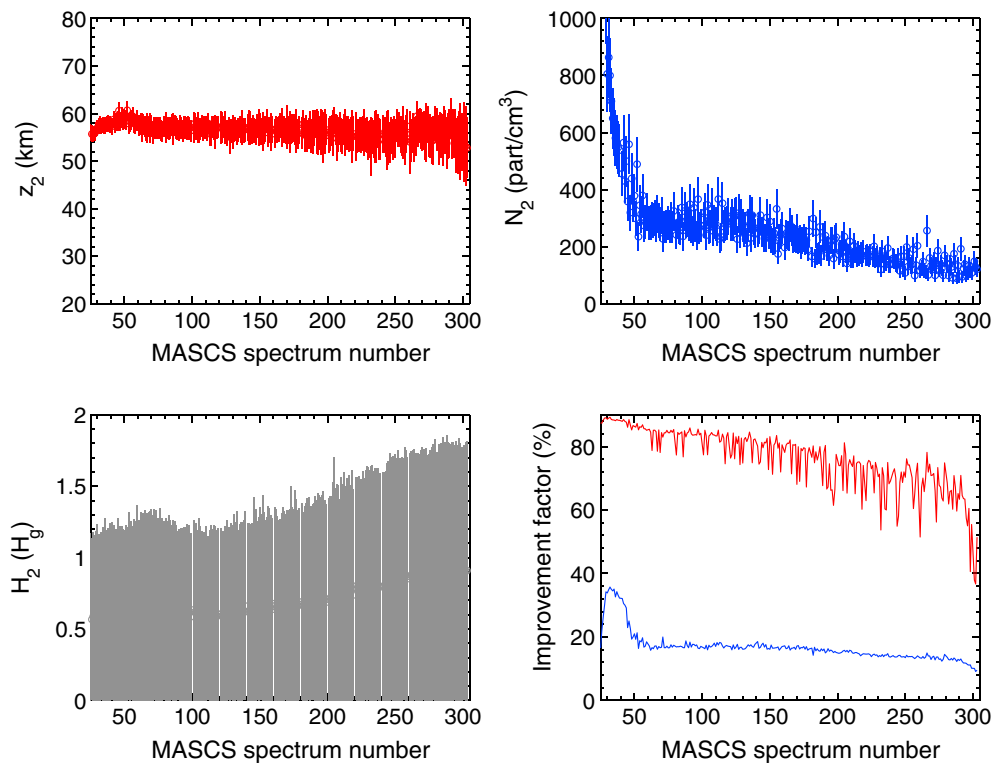
Figure 11. Model results for mode 2 particles parameters and improvement factor. Red line is used for the cloud base height z_2, blue line for the particle number density N_2, and gray for fractional scale height H_2, the scale height in terms of the gas scale height H_g.
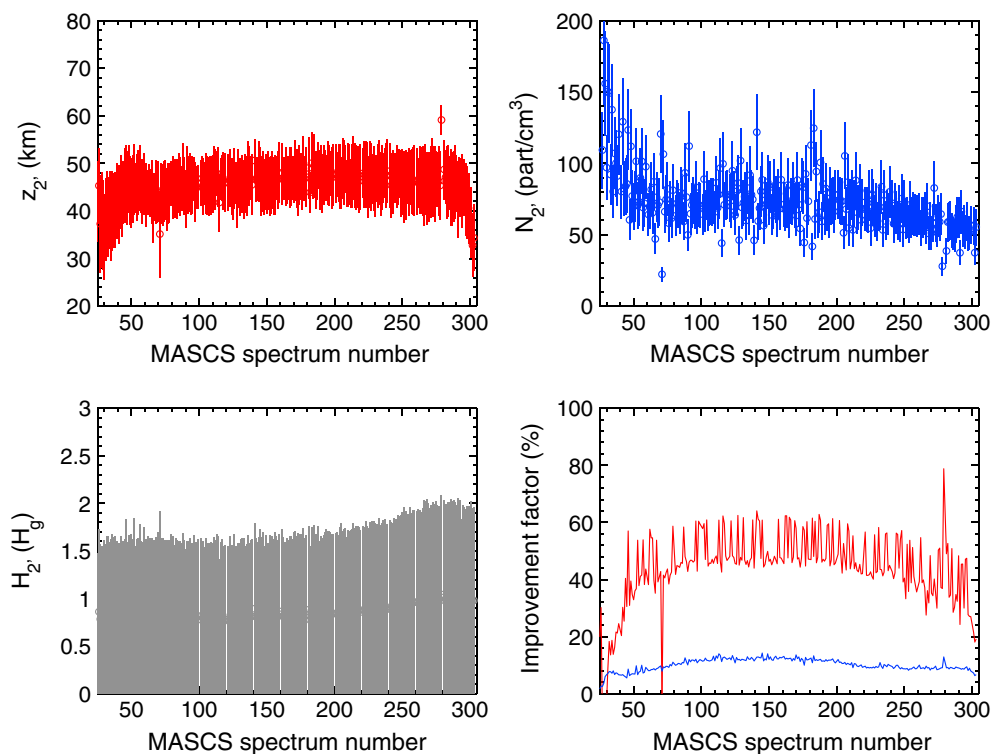
Figure 12. Model results for mode 2′ particles parameters and improvement factor. Red line is used for the cloud base height $z_{2'}$, blue line for the particle number density $N_{2'}$, and gray for fractional scale height $H_{2'}$, the scale height in terms of the gas scale height H_g.

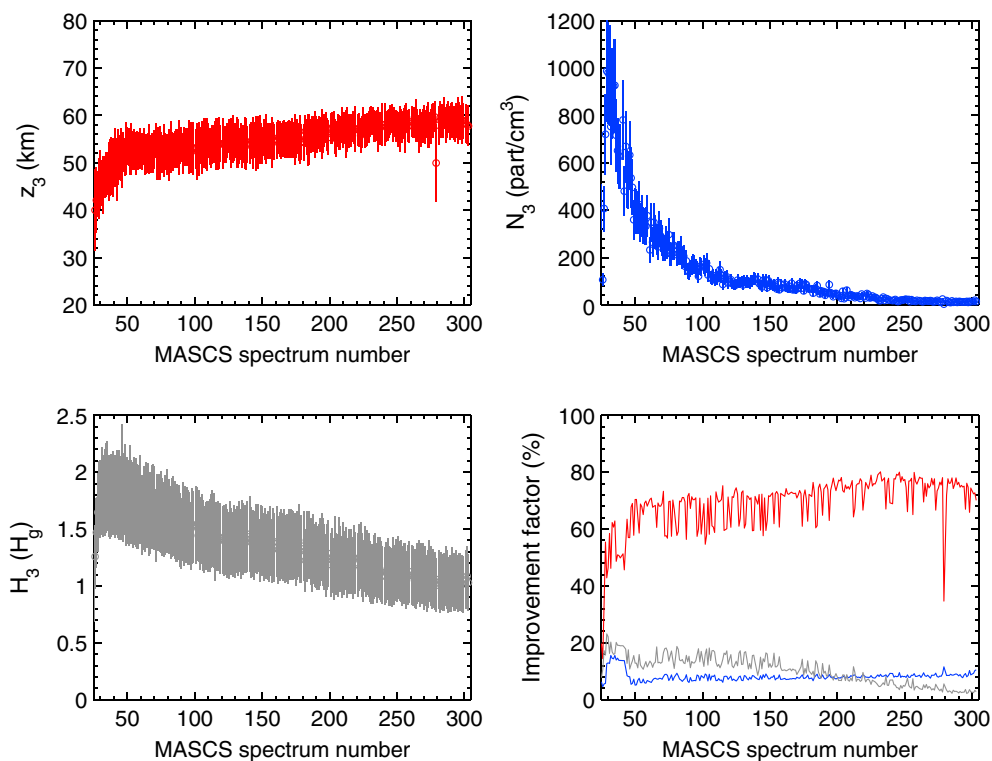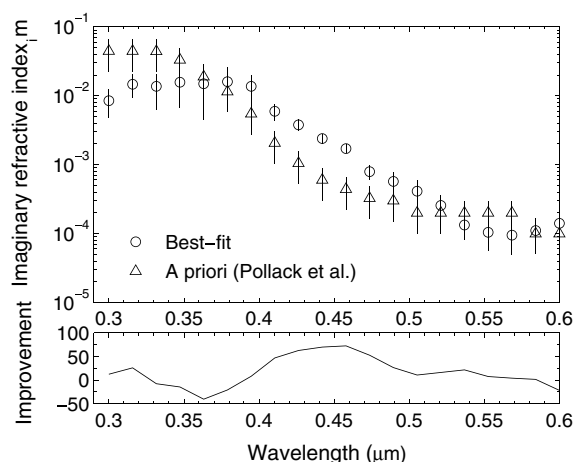**Figure 13.** Model results for mode 3 particles parameters and improvement factor. Red line is used for the cloud base height z_3, blue line for the particle number density N_3, and gray for fractional scale height H_3, the scale height in terms of the gas scale height H_g.

Figure 14. (top) Results for average imaginary refractive index m_i compared with a priori assumption from Pollack et al. (1980) and (bottom) improvement factor.

At the same time, the particle number density is reduced drastically from a maximum value of $\sim 1{,}000$ particles cm^{-3} to a few tens of particles cm^{-3} (average value of $N_3 = 70 \pm 60$ particles cm^{-3}). The scale height also changes from $H_3 \sim 2\,H_g$ to $1\,H_g$ (5–10 km) and an improvement factor around 20%. When combining these values in an integrated measure, the total optical thickness of mode 3 particles is fairly stable with a mean value of $\tau_3 = 7.5 \pm 0.4$. This suggests that more mode 3 particles are required in the higher atmosphere where our retrieval is the most sensitive, while it differs in the way of making this possible. At 70 km, for example, the particle concentration of mode 3 particles is N_3 (70 km) $= 1.6 \pm 0.3$ particle cm^{-3}, with slightly higher values at the last spectra but low dispersion in general.

4.3. UV Absorption

We show in Figure 14 the average results for the imaginary refractive index of mode 1 particles that fits the UV absorption. The real refractive index is computed from the reference values and fitted imaginary values using the Kramers-Kronig relations, as discussed in section 3.2. The resulting values of real parts do not depart significantly from the initial values less than 1%. Other works (Petrova et al., 2015; Rossi et al., 2015; Shalygina et al., 2015) were better suited for determining the real refractive index and found similar values.

The initial values of the imaginary refractive index by Pollack et al. (1980) can be described in terms of central wavelength absorption at 0.33 μm with a full width at half maximum slightly below 100 nm, if we assume that the absorption band follows a perfect Gaussian shape. These numbers must be taken cautiously as we only have information at one side of the absorption band and the few wavelengths in the short side might be affected by the SO_2 gas absorption as well.

Our results show a similar absorption to the prior derived by Pollack et al. (1980) but clearly displaced toward longer wavelengths, with maximum absorption at 0.34 μm and wider wings with full width at half maximum = 140 nm, again assuming that the absorption band is Gaussian. In Figure 14, we show the standard deviation of the values at each wavelength for all spectra, but retrieval errors are very similar in magnitude. As seen, results are more precise in the region from 0.4 to 0.45 μm, where the albedo rapidly increases for the central part of the absorption band. Values at the shortest wavelengths, where the absorption is the strongest, are more affected by the description of mode 1 particles (particle number density and height). With respect to the behavior at longer wavelengths (greater than 0.6 μm), the results suggest that the tail of the absorption continues. However, the difference in absorption is so low with such values of the imaginary refractive index that we cannot robustly conclude that this is the case. The tail of the absorption in the red and near-infrared side of the spectrum deserves further research as it can help to elucidate the origin of the UV absorption.

The retrieval differs significantly from the a priori values both at wavelengths below 0.35 μm (where our absorption is weaker) and in the region from 0.4 to 0.5 μm, where our particles absorb more strongly. This change in the particle absorption will be of interest when we discuss the nature of the UV absorber in the following section.

Our results are in good agreement with independent determinations such as Lee et al. (2017), where the most probable values of the imaginary refractive index were evaluated by fitting observations of the glory with Akatsuki/UVI 283 nm filter. In the simulations, the peak of the glory became clearer with values similar to the largest ones found in this work and the bottom of the UV absorber located at similar altitudes.

5. Discussion

5.1. Vertical Particle Distribution

A crude summary of the results presented in the preceding section can be found in Table 2. As long as our results do not depart much from the priors with respect to the vertical distribution of cloud particles, there is an obvious general agreement with the references they were based on. However, there are also a number of differences that are worth commenting on. First, our initial runs required the mode 1 to be located substantially higher than in the work by Barstow et al. (2012), with the mode 1 cloud base above 60 km rather than below 50 km. This is more in consonance with the description by Crisp (1986), as it has been already discussed. Second, the cloud base for our mode 3 particles tends to be located higher in the atmosphere than

Table 2
Summary of the Retrievals

Layer	Parameter	A priori	Best fitting
Mode 1	z_1 (km)	60	65 ± 2
	τ_1	4	3.2 ± 0.2
Mode 2	z_2 (km)	60	56 ± 1
	τ_2	8	10-5
Mode 2′	$z_{2'}$ (km)	45	46 ± 2
	$\tau_{2'}$	8	6.8 ± 0.4
Mode 3	z_3 (km)	45	55 ± 2
	τ_3	9	7.5 ± 0.4

in any previous work. This possibly implies the need of having more large-sized particles at higher altitudes (70 km), where our model is more sensitive. This could have been alleviated by incorporating absorption also on mode 2 particles, something that we discarded as an initial assumption but that could deserve further research.

We have computed the cloud top as the level at which the one-way total optical depth is $\tau = 1$ for wavelength of 0.63 μm, as in previous works. In spite of the dispersion of particular values for each particle mode, the value is remarkably constant among all spectra with a mean altitude of $z_{top} = 75 \pm 2$ km. This is very similar to the value of ~ 74 km given by Ignatiev et al. (2009) for the equatorial latitudes. The result by Lee et al. (2012) is lower ($\sim 67 \pm 2$ km), but it must be noted that this value is given at a longer wavelength (4.5 μm) and that only mode 2 particles were used in that model. The combination of both facts necessarily results in a cloud top at deeper level. However, Lee et al. (2012) finds a particle scale height similar to the gas scale height as we did.

One of the best references with respect to the vertical distribution of particles in the Venusian atmosphere is the work done with the Pioneer Venus particle size spectrometer experiment, described by Knollenberg and Hunten (1980). There is an overall agreement with the direct measurements of the Pioneer Venus probe, with smaller mode 1 particles showing abundances in the hundreds and larger mode 3 particles only in the tens of particles cm^{-3}. There is also a notable agreement with the mode 1 total optical thickness ($\tau_1 = 3.2 \pm 0.2$ in our work versus 3.23 in Knollenberg & Hunten, 1980, Table 5). However, the mode 2 in Knollenberg and Hunten (1980) accounts for an optical thickness of 9.76, while the combination of our mode 2 and mode 2′ is above $\tau_{2+2'} \gtrsim 12$ for most spectra. This is compensated by mode 3 particles, which in our results only account for half of the total optical thickness as they did in Knollenberg and Hunten (1980). However, we are not very sensitive to the distribution of mode 3 particles and the agreement with direct measurements is good in the levels around 65 km.

Regarding more recent results, comparing with the results by Molaverdikhani et al. (2012), we find that the number of mode 1 particles is about the same above the cloud base (located at 60 km in their work), although they retain some particle abundance down to 48 km, something that we do not include in our model. There are some discrepancies though, as they assume smaller particles for mode 1 and thus the mode 1 opacity should be lower in their model. In the case of mode 2 particles we have similar figures of the order of a few hundred particles cm^{-3}, but they are possibly higher in this work for most cases. This happens again with mode 3 particles: similar order of magnitude but slightly higher for our results. The integrated aerosol opacity in our case is around $\tau \sim 25$ at 0.63 μm, which seems close enough to typical estimations of the total particle load in the atmosphere (Esposito et al., 1997).

In the case of the hazes located in the upper atmosphere, works by Gao et al. (2013) and Luginin et al. (2016) dealt with the distribution of particles above the main cloud deck. Our results compare well with those by Luginin et al. (2016) at 75 km, where we find a mean of $\sim$100 particles cm^{-3} of mode 1 particles and $\sim$1.5 particles cm^{-3} of mode 2. This is comparable with their 500 particles cm^{-3} and 1 particle cm^{-3}, respectively. At 90 km, however, the agreement is poorer and we get about 1 order of magnitude fewer particles for both modes. As our sensitivity at those levels is very low, this difference is not conclusive and their values should be trusted.

All in all, the average vertical distribution of particles is typical of the equatorial region of Venus, with cloud tops higher than what is commonly retrieved at higher latitudes (Ignatiev et al., 2009). For the levels between 50 and 70 km, where we are the most sensitive, the results yield no surprises.

5.2. UV Absorber Candidates

There are a number of issues that must be studied in order to constrain the nature of the UV and blue absorber longward of 0.32 μm. First, any proposed candidate (or combination of them) should match the spectral signature of the UV absorber. Second, the expected number density of the candidate should be consistent with the already existing photochemical models at all the heights we are able to sound in the UV wavelengths. This includes the survival time of the candidate, which should also be in agreement with the dynamical scales observed in the UV markings (Titov et al., 2007): for spatial scales of thousands of kilometers, we can identify

Table 3
Candidates for UV Absorption

Candidate	Reference	Spectral data	χ^2
S_3	Toon et al. (1982)	Toon et al. (1982)	190
S_4	Toon et al. (1982)	Toon et al. (1982)	4×10^5
S_8 (25°C)	Hapke and Nelson (1975)	Toon et al. (1982)	120
S_8 (100°C)	Hapke and Nelson (1975)	Toon et al. (1982)	76
S_2O	Hapke and Graham (1989)	Lo et al. (2003)	14
OSSO	Frandsen et al. (2016)	Frandsen et al. (2016)	22
SCl_2	Krasnopolsky (1986)	Colton and Rayne (1974)	57
$(NH_4)_2S_2O_5$	Titov (1983)	Krasnopolsky (1986)	164
$NOHSO_4$	Watson et al. (1979)	Sill (1983)	928
Cl_2	Pollack et al. (1980)	Pollack et al. (1980)	76
$FeCl_3$	Krasnopolsky (1985)	Aoshima et al. (2013)	86
$C_5O_5H_2$	Hartley et al. (1989)	Bertaux et al. (1996)	1.5×10^4

clouds even after 4 days (Sánchez-Lavega et al., 2016). The planetary-scale dark markings created by the Kelvin wave responsible for the *Y* feature (i.e., the dark phase of the wave) can be tracked as it distorts progressively up to 30 days (Peralta et al., 2015; Rossow et al., 1980).

In this work, we will only focus on the spectral characterization of the candidates. We will follow the short list provided by Mills et al. (2007) of fewer than a dozen candidates, including the recent proposal by Frandsen et al. (2016). Table 2 and Figure 15 show some of these candidates together with the most early reference and the source of the spectral data to the absorption of each species. The last column (χ^2) is the mean quadratic deviation from our results including their uncertainty to each candidate's absorption, computed below 0.6 μm.
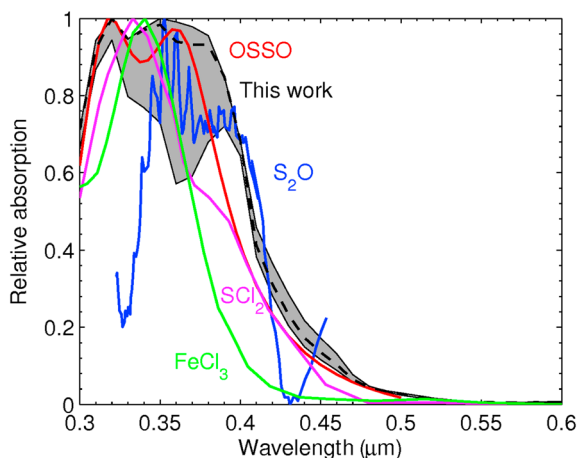
Some of the candidates do not match at all the observed UV absorption. Most notably, S_4 cannot account alone for the UV marking, which is obvious as its absorption is centered at longer wavelengths. The croconic acid ($C_5O_5H_2$) proposed by Hartley et al. (1989) and Bertaux et al. (1996) gives also a very bad spectral fit to our results, as happens with the nitrosulfuric acid proposed by Watson et al. (1979).

It must be noted that most of the candidates, though not all, could account for the core absorption around 0.35 μm (Figure 15). The main problem is fitting the spectral slope between 0.4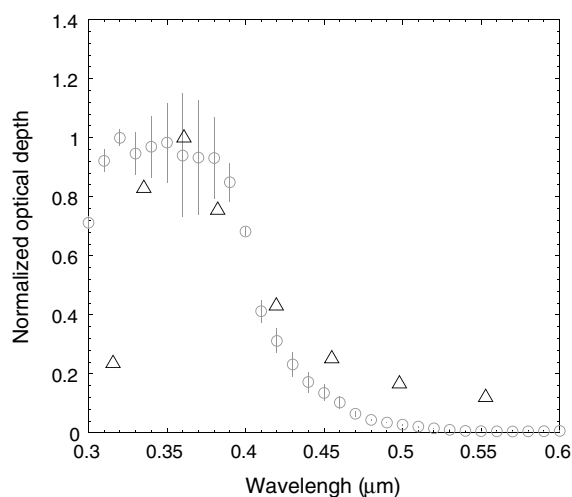 μm and 0.5 μm with a single component. The best agreement is found for an irradiated version of S_2O from Lo et al. (2003) (whose application to the Venus problem might not be straight-forward) and the recently proposed OSSO (Frandsen et al., 2016). Other species have a too narrow absorption to be in agreement with our results. This happens, for example, with SCl_2, Cl_2, or $FeCl_3$.

Figure 15. A comparison of the relative absorption (in arbitrary units) of some of the candidates for the UV absorber proposed so far with the model results obtained in this work. The gray area is used for our mode results, with the black dashed line being used for best fitting values, and maximum and minimum absorption values being indicated with solid black lines.

Even though the average deviation is lower for S_2O, the spectral shape of our results resembles that of OSSO better and therefore they support this candidate if we are to attribute the absorption to just one absorber. As most of the candidates depart from our results around at 0.4 μm, it is tempting to argue in favor of a second absorber that could complement the absorber in this range. In such a case, S_4 would be an excellent candidate. Some arguments have been provided so far against sulfur compounds (Krasnopolsky, 2016) and in favor of $FeCl_3$ (Krasnopolsky, 2017), but still, the spectral data are not close enough to support these species.

There are some uncertainties in this discussion. First, the assumed particle size has an effect on the width of the absorption band, with larger particles having a broader absorption. We have tested particle sizes from 0.1 μm to 0.5 μm, and this would partially mitigate the deviation of OSSO or SCl_2 but it is not enough for $FeCl_3$. In any case, such model dependency must be highlighted. Second, the spectral data for all candidates are still very dispersed in the literature and often presented in a number of ways that prevent a straightforward comparison.

Figure 16. Normalized optical thickness for the UV absorption in this work (gray circles with error bars) compared with parameterization by Haus et al. (2016) (black triangles).

Third, it would be desirable to have a better observational coverage of Venus spectrum from 0.35 μm to 0.5 μm. Fortunately, there is much information from VeX/VIRTIS that could be analyzed in the future and more recent observations from Akatsuki mission will help to correlate the variability of SO_2 and the UV absorber (Lee et al., 2017).

5.3. The Effect on Energy Budget

The vertical distribution of the UV absorber, together with its absorption spectrum, strongly influences the solar heating rates in Venus's mesosphere (Crisp, 1986). This effect was measured with the Solar Flux Radiometer (LSFR) experiment on the large probe of the Pioneer Venus mission (Tomasko et al., 1985). Recent works have analyzed the radiative energy balance of Venus (Haus et al., 2015, 2016; Lee, Imamura, et al., 2015) and, in particular, the role of the UV absorption in solar heating.

While it is beyond the scope of this paper to provide a complete analysis of the solar heating rates, we can still discuss our results in terms of the parameterizations used so far to reproduce the shortwave range of the energy budget. There are essentially two aspects that must be addressed to this regard: vertical distribution of the absorber and its absorption spectrum. The rest of the atmospheric parameters also have an influence but can be taken as second-order effects.

The vertical distribution of the UV absorber has been taken in this work to be tied to the distribution of mode 1 particles, as done by Crisp (1986). As shown in section 4.2, our retrievals give an average value of 65 ± 2 km for the base of mode 1 particles. This would be closer to or somewhat higher than the low UV absorber model in Haus et al. (2015, 2016). However, these works assume a scale height of 1 km, which is substantially lower than our ∼ 4 km scale height for mode 1. As this results in a cloud top, as previously defined, above 70 km, we argue that our results are closer to the nominal vertical distribution model by Haus et al. (2015, 2016). It must be noted that our approach is unable to determine the vertical distribution of UV absorber independently of mode 1. While other works have not been completely successful in confidently constraining the vertical distribution of the UV absorber, they suggest that the unknown UV absorber may be more concentrated right below the cloud tops, and the bottom should be not deeper than 60 km (Lee et al., 2017).

The second aspect of interest would be the spectral shape of the absorption itself. Here we will compare our results with those from Haus et al. (2016), shown in Figure 16. The optical thickness is given normalized to the maximum value, to make it independent of the assumption of UV absorber being attached to mode 1 particles. In this simple comparison we find that Haus et al. (2016) absorption is in general agreement with our results for the core of the absorption bands, but it is displaced toward red wavelengths. Absorption at 0.32 μm is significantly lower than ours, but it is higher at 0.5 μm.

If we convolve each curve with the solar flux, we find that the UV absorber by Haus et al. (2016) blocks 40% more flux than the one in our work, by direct absorption. This could result in an overestimation of the solar heating rates at these wavelengths. However, the solar flux scattered by each model should also be taken into account in order to make an accurate determination of the impact of our results in the solar heating rates. In fact, Lee, Imamura, et al. (2015) showed that models should consider important factors such as the vertical variations of the cloud top altitude (raising the cloud top from 67 to 70 km can increase the heating rate at the cloud tops about 50%) or the horizontal distribution of the UV absorber as they are responsible for about half of the total solar heating at the cloud tops.

6. Conclusions

In this work, we have analyzed spectra taken during the MESSENGER spacecraft's second Venus flyby on 5 June 2007. In particular, the spectra were taken by the instrument MASCS that covers from the near ultraviolet (0.3 μm) to the near infrared (1.49 μm). Such spectra have been modeled with a radiative transfer model that is able to fit the observed radiance as a function of wavelength using as free parameters the vertical distribution of Venusian particles and the imaginary refractive index of the UV absorber.

Our results show an equatorial atmosphere with very homogeneous properties (particularly cloud tops and total particle density), whose cloud tops are located at 75 ± 2 km, in good agreement with previous works. Our results are dominated by the particles located at 60 km or above, with little sensitivity below that.

The imaginary refractive index of the UV absorber is found to be blue shifted with respect to previous works, centered at 0.34 ± 0.03 μm with a full width at half maximum of 0.14 ± 0.01 μm if we assume a Gaussian shape for the absorption band. When comparing the spectral shape of the absorption with candidates proposed so far, we find that there is a better correlation with sulfur-bearing compounds such as S_2O or S_2O (in the form of OSSO *cis* and *trans* isomers), with SO_2 as a source, if we accept that the UV absorption is produced by a single compound. The change in the UV absorption may have an influence in the determination of the solar heating rates for Venus atmosphere that deserve future research.

The identification of the UV absorber is a problem far from being solved. While this work supports the spectral similarity of the retrieved values with disulfur dioxide, it must be noted that the vertical distribution assumed here is not in complete agreement with the profiles computed by Frandsen et al. (2016). A more recent work (Krasnopolsky, 2018) also shows the weaknesses of this explanation in view of state-of-the-art photochemical models of Venus's atmosphere.

As future work, there are essentially two aspects that should be investigated. Laboratory spectra of already proposed or new candidates for the UV absorption at the conditions of the upper Venus atmosphere (temperature, pressure, and solar radiation) are required. Middle- to high-resolution Venus spectra would also be welcome, particularly if they provide spatial resolution to separate regions with higher and lower UV absorption. The wavelength range of 0.4–0.5 μm is of the highest interest, as it may provide very useful constraints on the nature and composition of the UV absorption in Venus atmosphere. High-resolution spectra would also help to separate gaseous absorption from broader condensed matter absorption, thus constraining the physical state of the UV absorber.

References

Aoshima, H., Satoh, K., Umemura, T., & Kamigaito, M. (2013). A simple combination of higher-oxidation-state FeX_3 and phosphine or amine ligand for living radical polymerization of styrene, methacrylate, and acrylate. *Polymer Chemistry*, 4, 3554–3562.

Barstow, J. K., Tsang, C. C. C., Wilson, C. F., Irwin, P. G. J., McGouldrick, K., Drossart, P., . . . Tellmann, S. (2012). Models of the global cloud structure on Venus derived from Venus Express observations. *Icarus*, 217, 542–560.

Belton, M. J. S., Gierasch, P. J., Smith, M. D., Helfenstein, P., Schinder, P. J., Pollack, J. B., . . . Pilcher, C. B. (1991). Images from Galileo of the Venus cloud deck. *Science*, 253, 1531–1536.

Belyaev, D. A., Montmessin, F., Bertaux, J.-L., Mahieux, A., Fedorova, A. A., Korablev, O. I., . . . Zhang, X. (2012). Vertical profiling of SO_2 and SO above Venus' clouds by SPICAV/SOIR solar occultations. *Icarus*, 217, 740–751.

Belyaev, D. A., Evdokimova, D. G., Montmessin, F., Bertaux, J.-L., Korablev, O. I., Fedorova, A. A., . . . Luginin, M. S. (2017). Night side distribution of SO_2 content in Venus' upper mesosphere. *Icarus*, 294, 58–71.

Bertaux, J.-L., Widemann, T., Hauchecorne, A., Moroz, V. I., & Ekonomov, A. P. (1996). VEGA 1 and VEGA 2 entry probes: An investigation of local UV absorption (220–400 nm) in the atmosphere of Venus (SO_2 aerosols, cloud structure). *Journal of Geophysical Research*, 101, 12,709–12,745.

Bertaux, J.-L., Khatuntsev, I. V., Hauchecorne, A., Markiewicz, W. J., Marcq, E., Lebonnois, S., . . . Fedorova, A. (2016). Influence of Venus topography on the zonal wind and UV albedo at cloud top level: The role of stationary gravity waves. *Journal of Geophysical Research: Planets*, 121, 1087–1101. https://doi.org/10.1002/2015JE004958

Blackie, D., Blackwell-Whitehead, R., Stark, G., Pickering, J. C., Smith, P. L., Rufus, J., & Thorne, A. P. (2011). High-resolution photoabsorptionz cross-section measurements of SO_2 at 198 K from 213 to 325 nm. *Journal of Geophysical Research*, 116, E03006. https://doi.org/10.1029/2010JE003707

Boyer, C., & Camichel, H. (1961). Observations photographiques de la planète Venus. *Annales d'Astrophysique*, 24, 531–535.

Colina, L., Bohlin, R. C., & Castelli, F. (1996). The 0.12–2.5 μm absolute flux distribution of the Sun for comparison with solar analog stars. *The Astronomical Journal*, 112, 307–315. http://www.ajax.ehu.eus/sph/papers/2017JE005406/

Colton, R. J., & Rayne, J. W. (1974). Photoelectron and electronic absorption spectra of SCl_2, S_2Cl_2, S_2Br_2 and $(CH_3)_2S_2$. *Journal of Electron Spectroscopy and Related Phenomena*, 3, 345–357.

Crisp, D. (1986). Radiative forcing of the Venus mesosphere: I. Solar fluxes and heating rates. *Icarus*, 67, 484–514.

Crisp, D., Sinton, W. M., Hodapp, K.-W., Ragent, B., Gerbault, F., Goebel, J. H., . . . Stapelfeldt, K. R. (1986). The nature of the near-infrared features in the Venus night side. *Science*, 246, 506–509.

Ehrenheich, D., Vidal-Madjar, A., Widemann, T., Gronoff, G., Tanga, P., Barthélemy, M., . . . Arnold, L. (2012). Transmission spectrum of Venus as a transiting exoplanet. *Astronomy & Astrophysics*, 537, L2.

Esposito, L. W., Knollenberg, R. G., Marov, M. I., Toon, O. B., & Turco, R. P. (1983). The clouds are hazes of Venus. In D. M. Hunten, et al. (Eds.), *Venus* (pp. 484–564). Tucson, AZ: University of Arizona Press.

Esposito, L. W., Bertaux, J.-L., Krasnopolsky, V., Moroz, V. I., & Zasova, L. V. (1997). Chemistry of lower atmosphere and clouds. In Bougher, S. W., Hunten, D. M., & Philips, R. J. (Eds.), *Venus II: Geology, geophysics, atmosphere, and solar wind environment* (pp. 415–458). Tucson, AZ: University of Arizona Press.

Fedorova, A., Korablev, O., Vandaele, A.-C., Bertaux, J.-L., Belyaev, D., Mahieux, A., . . . Villard, E. (2008). HDO and H_2O vertical distributions and isotopic ratio in the Venus mesosphere by Solar Occultation at Infrared spectrometer on board Venus Express. *Journal of Geophysical Research*, 113, E00B22. https://doi.org/10.1029/2008JE003146

Frandsen, B. N., Wennberg, P. O., & Kjaergaard, H. G. (2016). Identification of OSSO as a near-UV absorber in the Venusian atmosphere. *Geophysical Research Letters*, *43*, 11,146–11,155. https://doi.org/10.1002/2016GL070916

Gao, P., Zhang, X., Crisp, D., Bardeen, C. G., & Yung, Y. L. (2013). Bimodal distribution of sulfuric acid aerosols in the upper haze of Venus. *Icarus*, *231*, 83–98.

García-Muñoz, A., & Mills, F. P. (2012). The June 2012 transit of Venus. Framework for interpretation of observations. *Astronomy & Astrophys.*, *547*, A22.

García-Muñoz, A., Wolkenberg, P., Sánchez-Lavega, A., Hueso, R., & Garate-Lopez, I. (2013). A model of scattered thermal radiation for Venus from 3 to 5 μm. *Planetary and Space Science*, *81*, 65–73.

García-Muñoz, A., Pérez-Hoyos, S., & Sánchez-Lavega, A. (2014). Glory revealed in disk-integrated photometry of Venus. *Astronomy Astrophys*, *566*, L1.

Hansen, J. E., & Hovenier, J. W. (1974). Interpretation of the polarization of Venus. *Journal of the Atmos. Sci.*, *31*, 1137–1160.

Hansen, J. E., & Travis, L. D. (1974). Light scattering in planetary atmospheres. *Space Science Reviews*, *16*, 527–610.

Hapke, B., & Nelson, R. (1975). Evidence for an elemental sulfur component of the clouds from Venus spectrophotometry. *Journal of the Atmospheric Sciences*, *32*, 1212–1218.

Hapke, B., & Graham, F. (1989). Spectral properties of condensed phases of disulfur monoxide, polysulfur oxide and irradiated sulfur. *Icarus*, *79*, 47–55.

Hartley, K. K., Wolff, A. R., & Travis, L. D. (1989). Croconic acid: An absorber in the Venus clouds? *Icarus*, *77*, 382–390.

Haus, R., Kappel, D., & Arnold, G. (2015). Radiative heating and cooling in the middle and lower atmosphere of Venus and responses to atmospheric and spectroscopic parameter variations. *Planetary and Space Science*, *117*, 262–294.

Haus, R., Kappel, D., Tellmann, S., Arnold, G., Piccioni, G., Drossart, P., & Häusler, B. (2016). Radiative energy balance of Venus based on improved models of the middle and lower atmosphere. *Icarus*, *272*, 178–205.

Hawkins III, S. E., Boldt, J., Darlington, E. H., Espiritu, R., Gold, R. E., Gotwols, B., ... Williams, B. (2007). The Mercury Dual Imaging System on the MESSENGER spacecraft. *Space Science Reviews*, *131*, 247–338.

Ignatiev, N. I., Titov, D. V., Piccioni, G., Drossart, P., Markiewicz, W. J., Cottini, V., ... Manoel, N. (2009). Altimetry of the Venus cloud tops from the Venus Express observations. *Journal of Geophysical Research*, *114*, E00B43. https://doi.org/10.1029/2008JE003320

Irwin, P. G. J., Teanby, N. A., de Kok, R., Fletcher, L. N., Howett, C., Tsang, C. C. C., ... Parrish, P. D. (2008). The NEMESIS planetary atmosphere radiative transfer and retrieval tool. *Journal of Quantitative Spectroscopy & Radiative Transfer*, *109*, 1136–1150.

Irwin, P. G. J., Tice, D. S., Fletcher, L. N., Barstow, J. K., Teanby, N. A., Orton, G. S., & Davis, G. R. (2015). Reanalysis of Uranus' cloud scattering properties from IRTF/SpeX observations using a self-consistent scattering cloud retrieval scheme. *Journal of Quantitative Spectroscopy & Radiative Transfer*, *109*, 1136–1150.

Khatuntsev, I. V., Patsaeva, M. V., Titov, D. V., Ignatiev, N. I., Turin, A. V., Limaye, S. S., ... Moissl, R. (2013). Cloud level winds from the Venus Express Monitoring Camera imaging. *Icarus*, *226*, 140–158.

Knollenberg, R. G., & Hunten, D. M. (1980). The microphysics of the clouds of Venus: Results from the Pioneer Venus particle size spectrometer experiment. *Journal of Geophysical Research*, *85*, 8039–8058.

Krasnopolsky, V. A. (1985). Chemical composition of Venus clouds. *Planetary and Space Science*, *33*, 109–117.

Krasnopolsky, V. A. (1986). *Photochemistry of the atmosphere of Mars and Venus*. Berlin: Springer-Verlag.

Krasnopolsky, V. A. (2006). Chemical composition of Venus atmosphere and clouds: Some unsolved problems. *Planetary and Space Science*, *54*, 1352–1359.

Krasnopolsky, V. A. (2016). Sulfur aerosol in the clouds of Venus. *Icarus*, *274*, 33–36.

Krasnopolsky, V. A. (2017). On the iron chloride aerosol in the clouds of Venus. *Icarus*, *286*, 134–137.

Krasnopolsky, V. A. (2018). Disulfur dioxide and its near-UV absorption in the photochemical model of Venus atmosphere. *Icarus*, *299*, 294–299.

Lee, Y. J., Titov, D. V., Tellmann, S., Piccialli, A., Ignatiev, N., Plätzold, M., ... Drossart, P. (2012). Vertical structure of the Venus cloud top from the VeRa and VIRTIS observations onboard Venus Express. *Icarus*, *217*, 599–609.

Lee, Y. J., Imamura, T., Schröeder, S. E., & Marcq, E. (2015). Long-term variations of the UV contrast on Venus observed by the Venus Monitoring Camera on board Venus Express. *Icarus*, *253*, 1–15.

Lee, Y. J., Titov, D. V., Ignatiev, N. I., Tellmann, S., Pätzold, M., & Piccioni, G. (2015). The radiative forcing variability caused by the changes of the upper cloud vertical structure in the Venus mesosphere. *Planetary and Space Science*, *113–114*, 298–308.

Lee, Y. J., Yamazaki, A., Imamura, T., Yamada, M., Watanabe, S., Sato, T. M., ... Murakami, S. (2017). Scattering properties of the Venusian clouds observed by the UV imager on board Akatsuki. *The Astronomical Journal*, *154*, 44–60.

Lo, W. J., Wu, Y.-J., & Lee, Y.-P. (2003). Ultraviolet absorption spectrum of cyclic S_2O in solid Ar. *The Journal of Physical Chemistry. A*, *107*, 6944–6947.

Luginin, M., Fedorova, A., Belyaev, D., Montmessin, F., Wilquet, V., Korablev, O., ... Vandaele, A. C. (2016). Aerosol properties in the upper haze of Venus from SPICAV IR data. *Icarus*, *277*, 154–170.

Marcq, E., Bertaux, J.-L., Montmessin, F., & Belyaev, D. (2013). Variations of sulphur dioxide at the cloud top of Venus's dynamic atmosphere. *Nature Geoscience*, *6*, 25–28.

McClintock, W. E., & Lankton, M. R. (2007). The Mercury Atmospheric and Surface Composition Spectrometer for the MESSENGER Mission. *Space Science Reviews*, *131*, 481–521.

McGouldrick, K., & Toon, O. B. (2007). An investigation of possible causes of the holes in the condensational Venus cloud using a microphysical cloud model with a radiative-dynamical feedback. *Icarus*, *191*, 1–24.

McNutt, R. L., Solomon, S. C., Grant, D. G., Finnegan, E. J., Bedini, P. D., & MESSENGER Team (2008). The MESSENGER mission to Mercury: Status after the Venus flybys. *Acta Astronautica*, *63*, 68–73.

Mills, F. P., Esposito, L. W., & Yung, Y. L. (2007). Atmospheric composition, chemistry and clouds. In *Exploring Venus as a terrestrial planet*. Washington, DC: American Geophysical Union.

Minnaert, M. (1941). The reciprocity principle in lunar photometry. *Astrophysical Journal*, *93*, 403–410.

Molaverdikhani, K., McGouldrick, K., & Esposito, L. W. (2012). The abundance and vertical distribution of the unknown ultraviolet absorber in the venusian atmosphere from analysis of Venus Monitoring Camera images. *Icarus*, *217*, 648–660.

Murray, B. C., Belton, M. J. S., Danielson, G. E., Davies, M. E., Gault, D., Hapke, B., ... Trask, N. (1974). Atmospheric motion and structure from Mariner 10 pictures. *Science*, *183*, 1307–1315.

Murtagh, F., & Heck, A. (1987). *Multivariate data analysis*. Netherlands: Reidel, Dordrecht.

Palmer, K. F., & Williams, D. (1975). Optical constants of sulfuric acid; Application to the clouds of Venus? *Applied Optics*, *14*, 208–219.

Peralta, J., Sánchez-Lavega, A., López-Valverde, M. A., Luz, D., & Machado, P. (2015). Venus's major cloud feature as an equatorially trapped wave distorted by the wind. *Geophysical Research Letters*, *42*, 705–711. https://doi.org/10.1002/2014GL062280

Peralta, J., Lee, Y. J., McGouldrick, K., Sagawa, H., Sánchez-Lavega, A., Imamura, T., . . . Nakamura, M. (2017). Overview of useful spectral regions for Venus: An update to encourage observations complementary to the Akatsuki mission. *Icarus*, *288*, 235–239.

Peralta, J., Lee, Y. J., Hueso, R., Clancy, R. T., Sandor, B. J., Sánchez-Lavega, A., . . . Peach, D. (2017). Venus's winds and temperatures during the Messenger's flyby: An approximation to a three-dimensional instantaneous state of the atmosphere. *Geophysical Research Letters*, *44*, 3907–3915. https://doi.org/10.1002/2017GL072900

Petrova, E. V., Shalygina, O. S., & Markiewicz, W. J. (2015). UV contrasts and microphysical properties of the upper clouds of Venus from the UV and NIR VMC/VEx images. *Icarus*, *260*, 190–204.

Pollack, J. B., Toon, O. B., Whitten, R. C., Boese, R., Ragent, B., Tomasko, M., . . . Wiedman, D. (1980). Distribution and source of the UV absorption in Venus' atmosphere. *Journal of Geophysical Research*, *85*, 8141–8150.

Pollack, J., Dalton, J., Grinspoon, D., Wattson, R., Freedman, R., Crisp, D., . . . Giver, L. (1993). Near-infrared light from Venus' nightside: A spectroscopic analysis. *Icarus*, *103*, 1–42.

Rodgers, C. D. (2000). *Inverse methods for atmospheric sounding, theory and practice*. London: World Scientific.

Ross, F. E. (1928). Photographs of Venus. *The Astrophysical Journal*, *68*, 57–92.

Rossi, L., Marcq, E., Montmessin, F., Fedorova, A., Stam, D., Bertaux, J.-L., & Korablev, O. (2015). Preliminary study of Venus cloud layers with polarimetric data from SPICAV/VEx. *Planetary and Space Science*, *113-114*, 159–168.

Rossow, W. B., Del Genio, A. D., Limaye, S. S., & Travis, L. D. (1980). Cloud morphology and motions from Pioneer Venus images. *Journal of Geophysical Research*, *85*, 8107–8128.

Rothman, L. S., Gordon, I. E., Babikov, Y., Barbe, A., Benner, D., Bernath, P. F., . . . Wagner, G. (2013). The HITRAN2012 molecular spectroscopic database. *Journal of Quantitative Spectroscopy and Radiative Transfer*, *130*, 4–50.

Sánchez-Lavega, A. (2011). *An introduction to planetary atmospheres*. FL: CRC Press Boca Raton.

Sánchez-Lavega, A., Peralta, J., Gómez-Forellad, J. M., Hueso, R., Pérez-Hoyos, S., Mendikoa, I., . . . Watanabe, S. (2016). Venus cloud morphology and motions from ground-based images at the time of the Akatsuki orbit insertion. *The Astrophysical Journal Letters*, *833*, L7.

Shalygina, O., Petrova, E. V., Markiewicz, W. J., Ignatiev, N. I., & Shalygin, E. V. (2015). Optical properties of the Venus upper clouds from the data obtained by Venus Monitoring Camera on-board the Venus Express. *Planetary and Space Science*, *113–114*, 135–158.

Sill, G. T. (1983). The clouds of Venus: Sulfuric acid by the lead chamber process. *Icarus*, *53*, 10–17.

Stamnes, K., Tsay, S.-C., Jayaweera, K., & Wiscombe, W. (1988). Numerically stable algorithm for discrete-ordinate-method radiative transfer in multiple scattering and emitting layered media. *Applied Optics*, *27*, 2502–2509.

Takagi, S., & Iwagami, N. (2011). Contrast sources for the infrared images taken by the Venus mission AKATSUKI. *Earth Planets and Space*, *63*, 435–442.

Titov, D. V. (1983). On the possibility of aerosol formation by the reaction between SO_2 and NH_3 in Venus. *Cosmic Research*, *21*, 401.

Titov, D. V., Taylor, F. W., Svedhem, H., Ignatiev, N. I., Markiewicz, W. J., Piccioni, G., & Drossart, P. (2007). Atmospheric structure and dynamics as the cause of ultraviolet markings in the clouds of Venus. *Nature*, *456*, 620–623.

Titov, D. V., Markiewicz, W. J., Ignatiev, N. I., Song, L., Limaye, S. S., Sánchez-Lavega, A., . . . Moissl, R. (2012). Morphology of the cloud tops as observed by the Venus Express Monitoring Camera. *Icarus*, *217*, 682–701.

Tomasko, M. G., Doose, L. R., Smith, P. H., & Odell, A. P. (1980). Measurements of the flux of sunlight in the atmosphere of Venus. *Journal of Geophysical Research*, *85*, 8167–8186.

Tomasko, M. G., Doose, L. R., & Smith, P. H. (1985). The absorption of solar energy and the heating rate in the atmosphere of Venus. *Advances in Space Research*, *5*, 71–79.

Toon, O. B., Turco, R. P., & Pollack, J. B. (1982). The ultraviolet absorber on Venus: Amorphous sulfur. *Icarus*, *51*, 358–373.

Tsang, C. C. C., Irwin, P. G. J., Taylor, F. W., & Wilson, C. F. (2008). A correlated-k model of radiative transfer in the near-infrared windows of Venus. *Journal of Quantitative Spectroscopy & Radiative Transfer*, *109*, 1118–1135.

Tsang, C. C. C., Wilson, C. F., Barstow, J. K., Irwin, P. G. J., Taylor, F. W., McGouldrick, K., . . . Svedhem, H. (2010). Correlations between cloud thickness and sub-cloud water abundance. *Geophys Research Letters*, *37*, L02202. https://doi.org/10.1029/2009GL041770

Vandaele, A. C., Korablev, O., Belyaev, D., Chamberlain, S., Evdokimova, D., Encrenaz, T., . . . Wilquet, V. (2017). CSulfur dioxide in the Venus atmosphere: I. Vertical distribution and variability. *Icarus*, *295*, 16–33.

von Zhan, U., & Moroz, V. I. (1983). Composition of the Venus atmosphere below 100 km. *Advances in Space Research*, *5*, 173–195.

Watson, A. J., Donahue, T. M., Stedman, D. H., Knollenberg, R. G., Ragent, B., & Blamont, J. (1979). Oxides of nitrogen and the clouds of Venus. *Geophysical Research Letters*, *6*, 743–746.

Zasova, L. V., Krasnopolsky, V. A., & Moroz, V. I. (1981). Vertical distribution of SO_2 in upper cloud layer of Venus and origin of the U.V.-absorption. *Advances in Space Research*, *1*, 13–16.

Zasova, L. V., Ignatiev, N., Khatuntsev, I., & Linkin, V. (2007). Structure of the Venus atmosphere. *Planetary and Space Science*, *55*, 1712–1728.